Double-Well Colloidal Nanocrystals Featuring Two-Color Photoluminescence.

Natalia Razgoniaeva,[1,2] *Mingrui Yang,*[1,2] *Cooper Colegrove,* [1,2] *Natalia Kholmicheva,*[1,2]
Pavel Moroz,[1,2] *Holly Eckard,*[1,3] *Abigail Vore,*[1,3] *Mikhail Zamkov*[1,2,*].

The Center for Photochemical Sciences[1], Department of Physics[2], Department of Chemistry,[3]
Bowling Green State University, Bowling Green, Ohio 43403.

* zamkovm@bgsu.edu

RECEIVED DATE (to be automatically inserted after your manuscript is accepted if required)

Ratiometric sensing strategy relies on the ratio of the two photoluminescence (PL) signals originating from the same nano-object for detecting the changes in the surrounding media. Recently, such dual-color emission has been demonstrated in semiconductor colloids, where the PL signal from a quantum-confined domain was complemented with the secondary emission from transition metal ions or a bulk-like structure. Here, we report on the development of dual-color nanocrystal colloids featuring a combination of two quantum-confined emitters within the same nano-object. The reported morphology relies on double-well core/barrier/shell arrangement, where zero-dimensional excitons of the core component (PbS) can coexist with two-dimensional excitons of the shell domain (CdSe). As a result, the core and shell emission bands can be independently tuned across 880–1500 nm and 600-650 nm spectral windows, respectively. A CdS potential barrier at the PbS/CdSe interface was designed to suppress the energy and charge diffusion between the two domains allowing both emission bands to exhibit quantum yields over 10%. Fabricated colloids were demonstrated as dual-color probes for sensing the redox environment, where both the energetics and the timing of photoinduced charge transfer to an add-on analyte could be inferred from the ratiometric measurements.

Dual-color emitting fluorophores have attracted a considerable amount of attention as ratiometric phosphors for sensing applications. The intensity ratio of the two emission bands originating from different recombination processes within the same nano-object has been demonstrated to depend on such environmental factors as the pH balance in the surrounding media,[1-5] gas pressure,[6] and the solvent temperature.[7,8] In this regard, semiconductor nanocrystals offer a unique perspective by enabling two-color photoluminescence with spectrally separated emission bands in both visible and infrared spectral windows.[8],[9-25] The photostability of inorganic colloids offers another important benefit for the development of sensor applications, as it facilitates a long-term exposure of phosphors to photodegrading environments.

Conventionally, the sensing strategy based on a dual-color emission in nanocrystals is enabled through a nanoparticle morphology where one emission band is originated from a quantum-confined component of a nanostructure while the other is produced by a quasi-confined domain or transition metal ions. According to this classifications, the plethora of nanocrystal morphologies developed for ratiometric sensing can be categorized into two types. The first architecture relies on integrating Mn^{2+} or Cu^{+} ions within a semiconductor nanocrystal body, allowing the emission of the dopant to be spectrally-separated from the thermally-activated emission of the nanocrystal host.[7,9,26,27] The resulting PL spectra reveal the two distinguishable peaks in the visible range, which ratio shows a predictable temperature dependence.[7,28-30] The second nanocrystal morphology that supports a dual-color emission is realized *via* spatially separated inorganic domains placed within the same nanoparticle, often in a core/shell configuration.[10-13,18] In this case, the simultaneous emission from the core (e.g. CdSe or PbSe) and the shell (e.g. wurtzite CdS) domains is enabled by a naturally forming potential barrier associated with an intermediate layer (zinc-blend CdS) at the interface of the core and the giant shell components. Such dual-color core/shell nanocrystals have been demonstrated as pH sensitive probes in aqueous media.[11]

The two aforementioned morphologies developed for dual-color nanocrystal probes were designed to support the quantum confinement in one of the two emitting domains, which brings an added advantage of a size-tunable emission wavelength and an enhanced PL quantum yield. Achieving the quantum confinement simultaneously in both emitting domains, however, has not yet been reported. The difficulty lies in the underlying synthetic challenge of placing two strongly confining components within the same nanoparticle. At the present state of the art, only a partial confinement corresponding to the localization of one of the two carriers has been realized in the secondary emissive domain though the use of a giant core/shell geometry. An incomplete confinement was noted to promote the diffusion of excitons or carriers into the other emissive domain or towards nanocrystal boundaries ultimately leading to a low emission quantum yield, short excited state lifetimes, and limited PL spectral tuning.

Here, we report on the synthesis and characterization of dual–emitting PbS/CdS/CdSe core/barrier/shell nanocrystals featuring confined excitons in the core (PbS) and the shell (CdSe) domains. To achieve a size-tunable photoluminescence from the shell component, we have employed a recently reported nanoshell deposition strategy[31] to grow a layer of the CdSe semiconductor onto PbS/CdS core/shell seeds. The resulting CdSe domain was shown to support two-dimensional excitons manifested through the size-dependent emission tunable *via* the shell thickness. The zero-dimensional excitons of a PbS core domain were spatially separated from the CdSe layer by means of a CdS barrier allowing the core and the shell emission bands to be independently tuned across 880 – 1500 nm and 600-650 nm spectral windows, respectively (Fig. SF1). The presence of a thick CdS potential barrier at the PbS/CdSe interface was also found to be effective in suppressing the energy and charge diffusion between the two domains allowing both emission bands to exhibit quantum yields of over 10%. The feasibility of ratiometric sensing with fabricated PbS/CdS/CdSe nanocrystals was explored through concentration measurements of cationic (MV^{2+}) and anionic (thiols) species in solution. Both the energetics and the temporal dynamics of photoinduced charge transfer to an add-on molecule was successfully inferred from the ratiometric measurements.

RESULTS AND DISCUSSION

Conjoining the two spatially-separated potential energy minima within a small-size colloidal nanostructure is a challenging task. Both the inter-domain exciton diffusion and charge carrier tunneling between the two potential wells can result in the suppressed excitation in one of the emission bands. Such excitation energy exchange is exemplified in the case of giant CdSe/CdS dual-emitting nanoparticles, which rely on a zinc blende CdS interstitial potential barrier to suppress the hole exchange between the CdSe core and the wurtzite CdS shell domains. Due to an offset in ionization energies of zinc blende (ZB) and wurtzite (WZ) CdS crystalline phases, the ZB CdS interstitial layer could serve as a 0.03-0.04 eV potential barrier to photoinduced holes in the shell.[12] This type of band alignment, however, offered no potential barrier to photoinduced electrons in the shell allowing those to delocalize across the entire CdSe/CdS$_{ZB}$/CdS$_{WZ}$ nanostructure. As a result, the lifetime of excitons in the shell limited to a picosecond range, leading to CdS PL quantum yield (QY) of only 0.1%.[10]

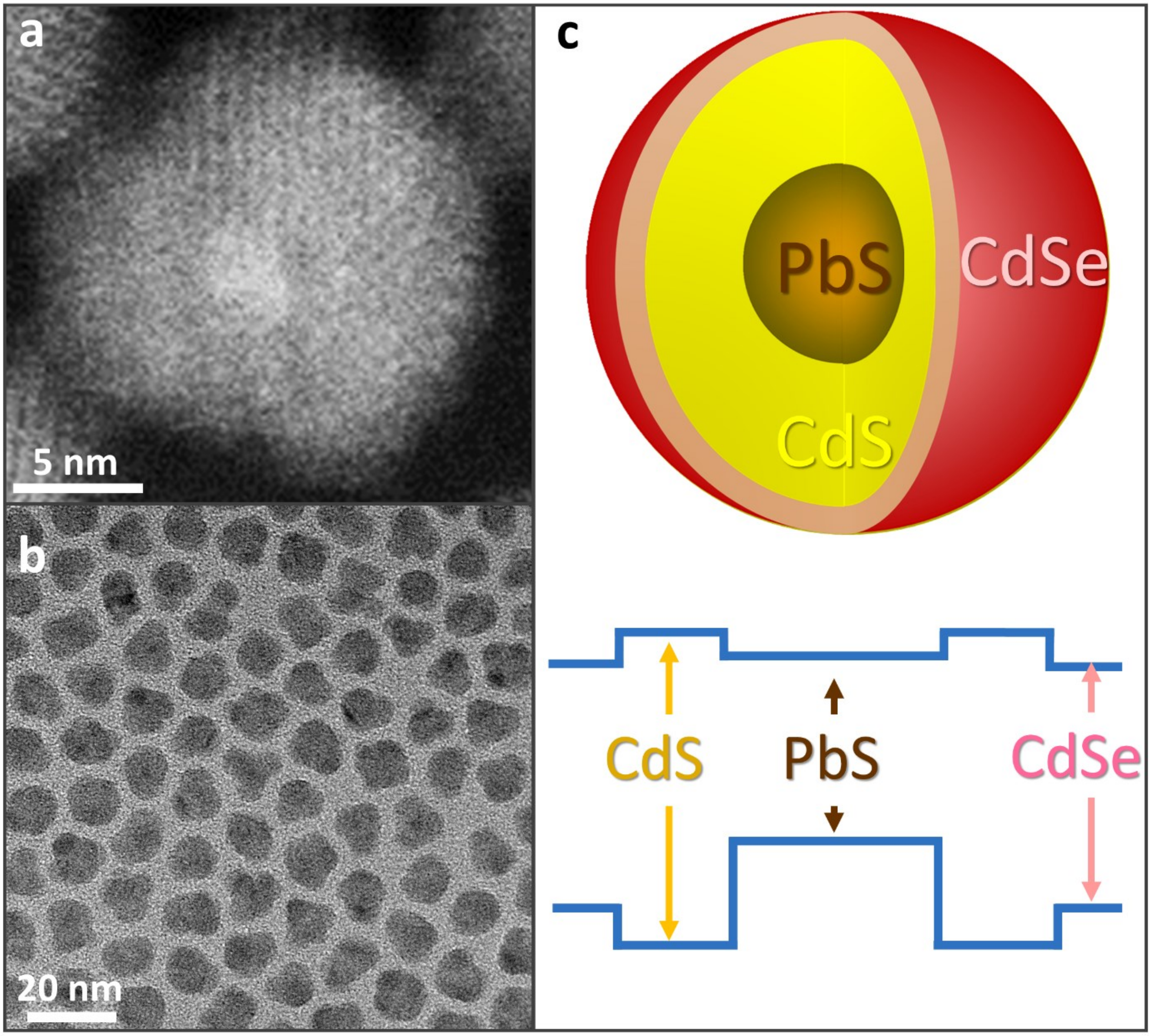

Figure 1. PbS/CdS/CdSe nanocrystal design for a dual-color emission. (a). Dark field STEM image of a PbS/CdS/CdSe nanocrystal indicating the presence of the PbS and CdSe domains through a color contrast. A somewhat darker shading around a bright center area is ascribed to be a CdS barrier. (b).

Low-resolution TEM image of PbS/CdS/CdSe NCs. (c). Schematic representation of excited state energy levels in fabricated core/barrier/shell NCs.

In the present work, the combination of the interstitial barrier (CdS) and emissive domains (PbS, CdSe) was chosen to provide a substantial localization for both electrons and holes in the two fluorescent components. The energy diagram in Figs. 1c and 5 illustrates the expected energy offsets in fabricated PbS/CdS/CdSe hetero-nanocrystals featuring 4.5-nm PbS core and 2.5-thick CdSe shell components. The proposed carrier localization in PbS and CdSe domains was initially assessed based on the evolution of optical properties observed during the nanocrystal growth (Fig. 2), which included two sequential steps. First, CdS shell was grown onto PbS core NCs *via* the $Cd^{2+} \rightarrow Pb^{2+}$ cation exchange.[32] Solvent temperatures of over 160 ºC and long reaction times (up to 10 hours) were used to reach an equilibrium diffusion of Cd^{2+} cations corresponding to the maximum permeation of Cd^{2+} cations into the original PbS core NCs. This strategy helped stabilizing the size of the PbS core within the CdS shell for the subsequent high-temperature CdSe deposition. The replacement of surface Pb^{2+} ions with Cd^{2+} gave rise to a characteristic blue-shift of the nanocrystal absorption edge (1250 nm → ~ 850 nm), corresponding to the deposition of 0.8-nm of the CdS shell. The resulting PbS/CdS NCs showed a strong emission in the 910-950 nm range (Fig. SF2), which intensity (QY ≈ 16%) and lifetime (> 1 μs) were consistent with a quasi-type I band edge alignment between core and shell domains. Such energetics is expected when the size of the PbS domain is around 3 nm in diameter in which case an excited electron is likely delocalized but yet partly confined in the core.[33-35] The subsequent deposition of the CdSe shell onto PbS/CdS NCs resulted in the onset of the shell emission at ~ 600 nm (Fig. 2b). The initial intensity of this band was low, which is likely the result of CdSe CB edge being above that of the CdS barrier. With increasing shell thickness, the intensity of the shell photoluminescence has intensified and red-shifted (Fig. 2b) in a manner consistent with the reduction in the CdSe CB energy relative to CdS CB. Indeed, since the effective electron mass in CdSe is about 3 times lower than that of holes, the band gap reduction with growing NC size is realized mostly by the changes in the CB band edge, promoting an electron localization in the CdSe shell (Fig. 1c). Accordingly, the emission of fully grown PbS/CdS/CdSe structures has a strong contribution from the CdSe shell domain with associated QY of 12.1%. Meanwhile, the emission of the PbS core becomes somewhat reduced during the high-temperature CdSe deposition, resulting in the final PbS QY of 10.5%.

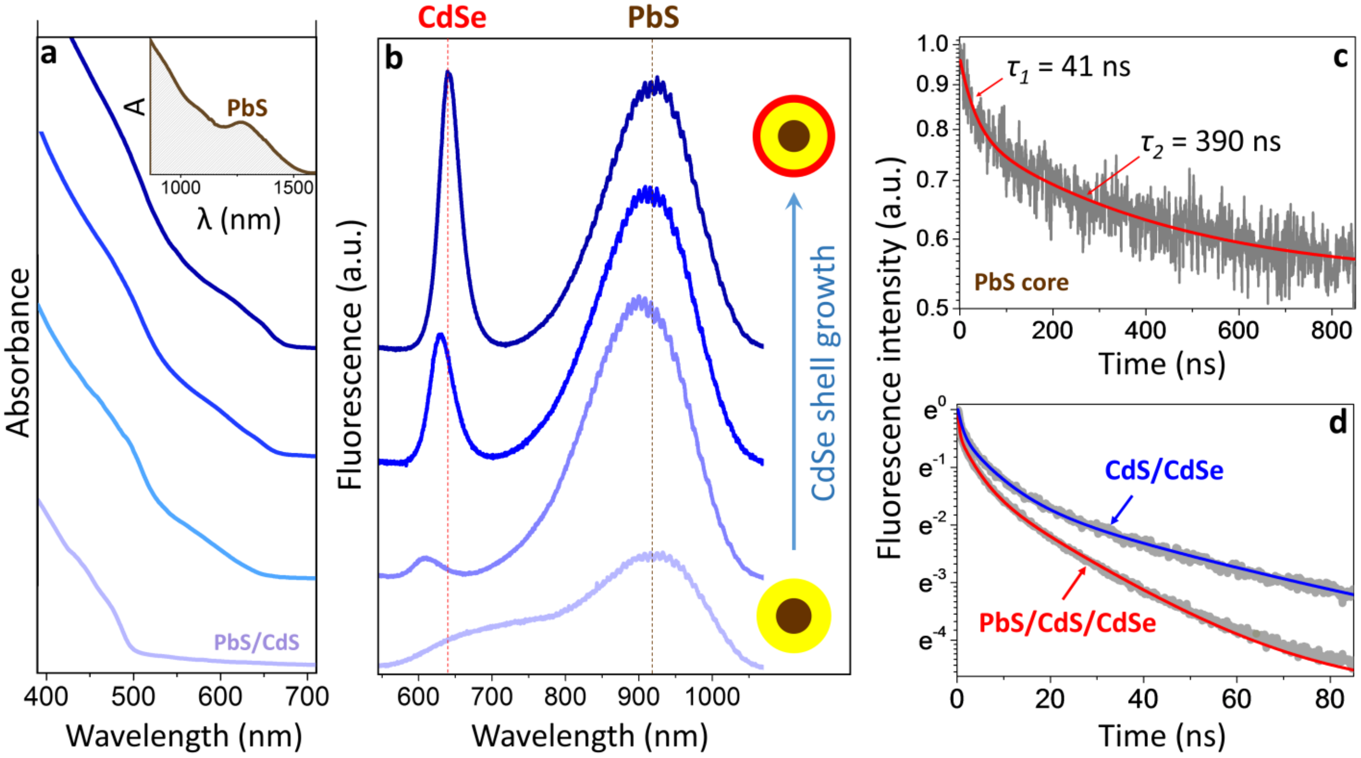

Figure 2. Optical properties of PbS/CdS/CdSe nanocrystals. (a). The evolution of absorption spectra corresponding to progressive stages of the CdSe shell deposition on PbS/CdS core nanocrystals. The absorption profile of PbS core NCs used for the synthesis of PbS/CdS core/shell nanoparticles *via* $Pb^{2+} \rightarrow Cd^{2+}$ cation exchange is shown in the insert. (b). The evolution of the PbS/CdS/CdSe photoluminescence spectra accompanying the deposition of the CdSe shell. With the increasing CdSe layer thickness, the corresponding CdSe band gap emission red-shifts and intensifies. (c). The lifetime of the PbS "core" emission of fully-grown PbS/CdS/CdSe NCs filtered using a long-pass filter, LP850. The decay is two-exponential with fast and slow times of 41 and 390 ns, respectively (amplitude-averaged τ_{av} = 346 ns). (d). A comparison of the CdSe "shell" photoluminescence lifetimes for

nanostructures with (red) and without (blue) the PbS core domain. A short-pass filter (SP700) was used in the former case to suppress the PbS emission. The reduction of the CdSe PL lifetime in PbS-seeded nanoparticles is consistent with the shell-to-core energy (charge) transfer. We estimate the efficiency for CdSe-to-PbS excitation transfer to be $E = 1 - \tau_{donor-acceptor} / \tau_{acceptor} \approx 52\%$.

The analysis of the PL lifetimes corresponding to the two emissive bands sheds further light on the photoinduced carrier confinement in fabricated double-well structures. According to Fig. 2c, the emission of the core resulting from 420 nm excitation exhibits a double exponential character with the amplitude-averaged exciton lifetime of 346 ns. For comparison, the PL lifetime of isolated PbS/CdS NCs is 1.2 microsecond, suggesting a possible contribution of trapping or tunneling deexcitation processes in PbS/CdS/CdSe that enhance the PbS($1S_e$) decay rate. The lifetime of excitons in the CdSe shell domain of PbS/CdS/CdSe NCs was found to exhibit a multi-exponential behavior (red curve, Fig. 2d), which value was determined using a three-exponent averaging fit[36] (τ = 15.9 ns). For a comparison, the lifetime of CdS/CdSe nanoshell samples (a characteristic TEM image is shown in Fig. SF6) fabricated without PbS core domains[31] was τ = 33.2 ns (Fig. 2d, blue curve). The reduced lifetime of the PbS-seeded dots is consisted with CdSe-to-PbS energy (or charge) transfer with the corresponding efficiency of $E = 1 - \tau_{donor-acceptor} / \tau_{acceptor} = 1 - 15.9/33.2 \approx 52\%$.

The dark-field STEM analysis of dual-emitting PbS/CdS/CdSe NCs in Fig. 3 reveals the presence of two distinct nanoparticle morphologies. According to Figs. 3a and 3b, the CdSe shell (brighter shading) can grow either in a Janus geometry with a single arm nucleating at the CdS surface (Fig.3a) or as a spherically symmetric layer with tetrapod-like twinning of CdSe (Fig. 3b). The location of the PbS core domain can be identified in both cases as a small bright area in the center of the darker-shaded CdS shell. The ratio of Janus to tetrapod-like morphologies in a particular batch depended on the synthetic conditions, however, a combination of both structural types was found in all investigated samples. The average diameter of PbS/CdS core/shell NCs was determined from bright-field TEM images in Fig. SF3 to be 4.6 nm, which is in a good agreement with estimates based on the exciton absorption edge in the starting PbS dots (Fig. 2a). Based on the measured 9.5-nm diameter of fully grown spherical PbS/CdS/CdSe nanocrystals, we estimate that the average thickness of the CdSe shell was 2.5 nm.

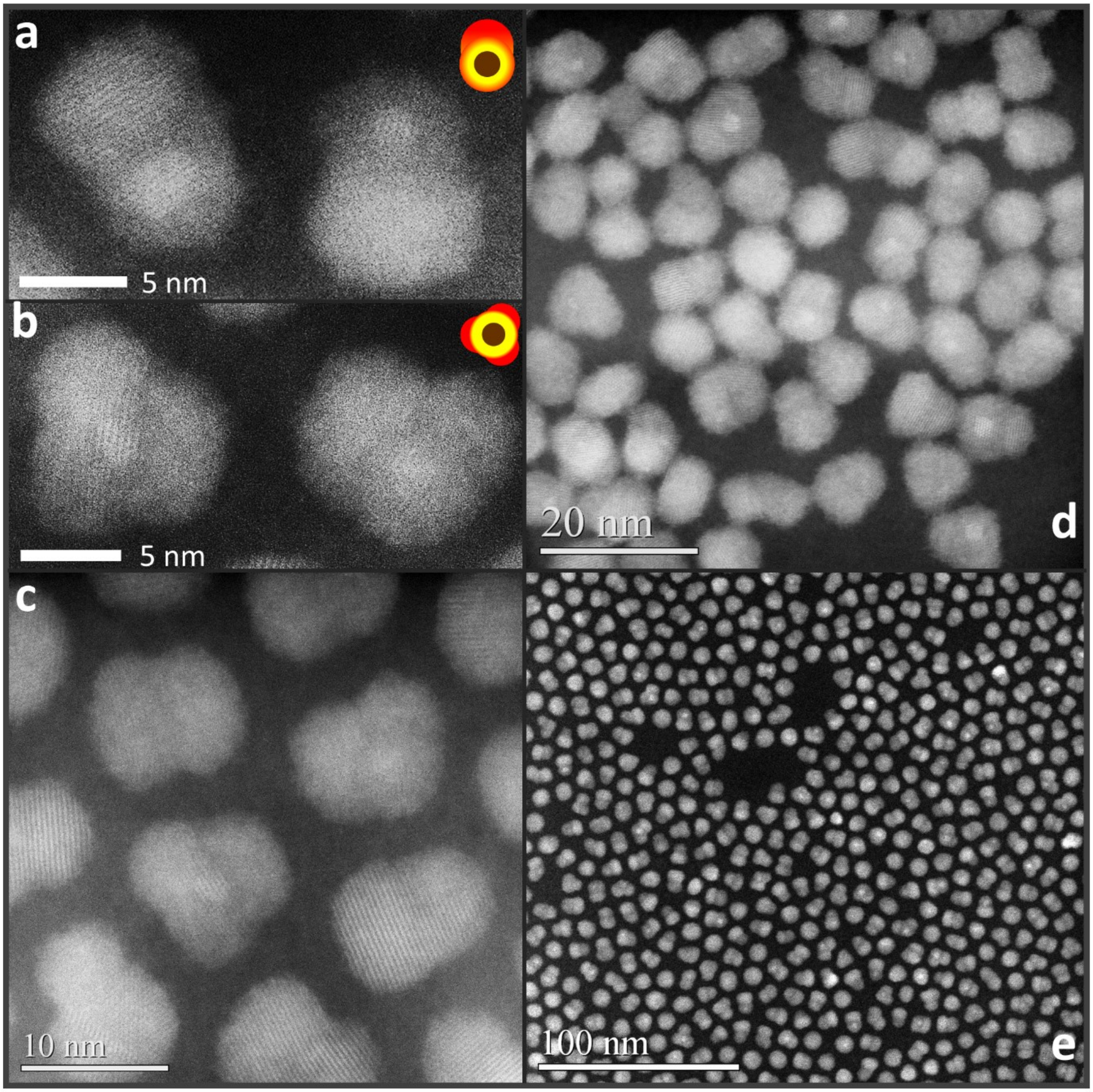

Figure 3. Dark-field scanning transmission electron microscope (STEM) images of PbS/CdS/CdSe nanocrystals. (a). A high-resolution color-contrast STEM image of Janus-type PbS/CdS-CdSe heterostructures indicating the presence of a (bright) CdSe domain on one side of a PbS/CdS core. The

location of PbS NCs is observed as a small bright area in the center of the structure. (b). Spatially symmetric PbS/CdS/CdSe nanocrystals showing a tetrapod-like growth of the CdSe shell. (c). STEM image showing the presence of both Janus and tetrapod-like PbS/CdS/CdSe nanocrystal morphologies in the same batch. (d,e). A low-magnification STEM images of PbS/CdS/CdSe nanocrystals. The location of PbS core domains can be identified in a few specimens through a color-contrast.

The X-ray powder diffraction (XDR) analysis of PbS/CdS/CdSe nanocrystals provides additional evidence in favor of the CdSe shell growth. According to Fig. 4, the original PbS/CdS core nanoparticles are predominantly in the ZB CdS crystallographic phase, which is consistent with previous reports on this semiconductor combination.[37] Indeed, the initial growth of the CdS shell onto PbS seeds forces the CdS layer to adopt the rock salt phase of the PbS core. However, when the shell thickness exceeds ~1.3 nm, the crystallographic phase of the growing CdS layer returns to an equilibrium zinc blende (see Fig. SF4). In present experiments, CdS shell was deposited through a cation exchange at high temperature for a duration of 10 hours which gave rise to a predominantly ZB CdS diffraction pattern (Fig. 4b). Following the deposition of the CdSe outer layer, the Bragg lines shift to a lower angle consistent with the increasing lattice spacing in ZB CdSe (Fig. 4a). Interestingly, the final product exhibits an averaged CdS/CdSe lattice spacing, which may suggest that some strain is present in the shell domain. This trend has been previously observed in the XRD pattern of spherical CdS/CdSe nanoshells that despite a larger volume fraction of CdSe in the outer layer showed a strained CdS/CdSe phase.[31]

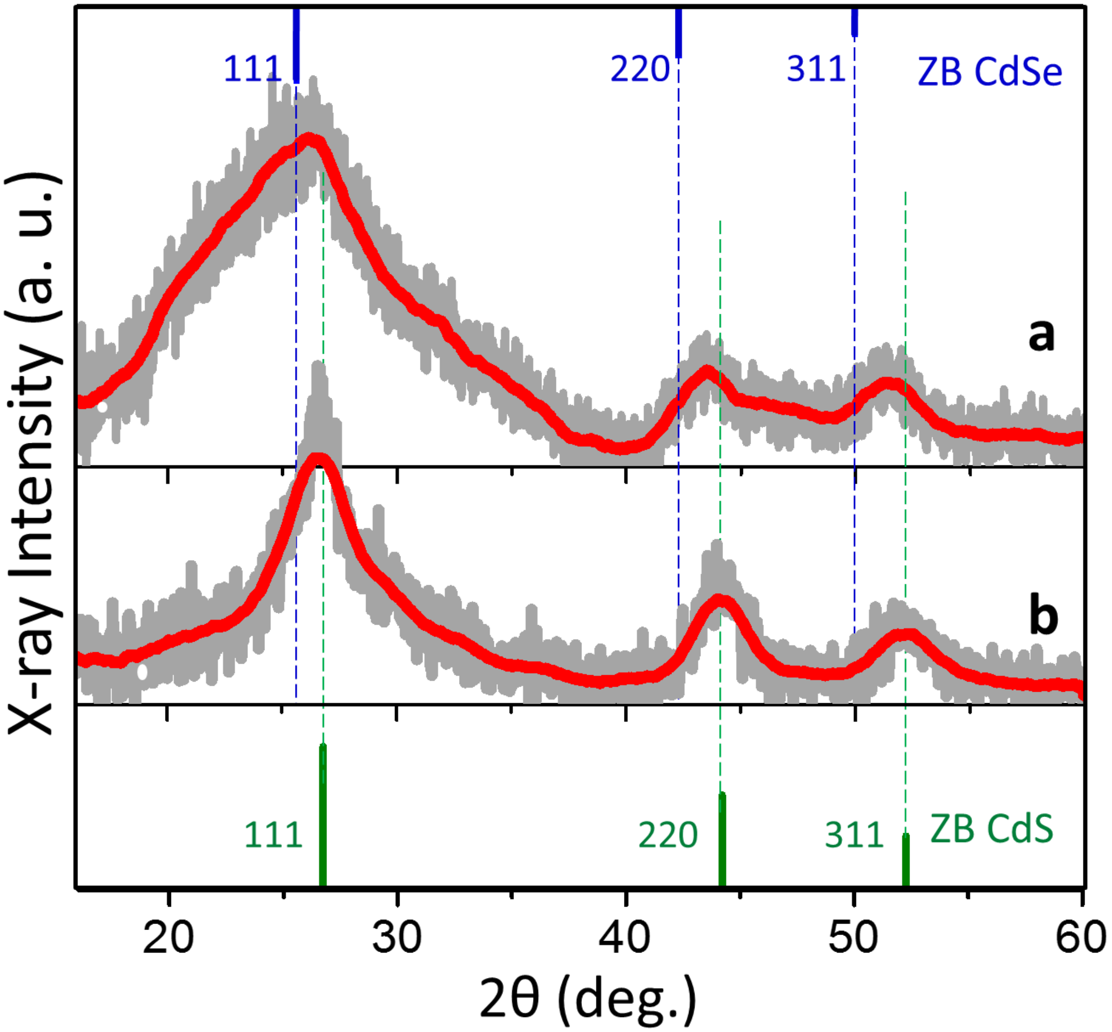

Figure 4. X-ray powder diffraction pattern of (a) - PbS/CdS/CdSe dual-emitting NCs, and (b) -PbS/CdS core/shell NCs prior to shell deposition. The growth of the CdSe layer onto zinc blende CdS results in a global shift of the corresponding Bragg peaks toward lower angles.

The feasibility of ratiometric sensing with fabricated PbS/CdS/CdSe nanocrystals was explored through concentration measurements of cationic and anionic species in solution. As a representative example of cations, methyl viologen (MV^{2+}) was introduced at various concentrations to nanocrystal samples in chloroform. MV^{2+} is a known reducing agent that can bind to surfaces of chalcogenide semiconductors through two reaction mechanisms: (i) - direct adsorption to exposed surfaces, and (ii) - adsorption through displacement of weakly bound Cd-oleate complexes.[38] Upon binding to surfaces,

MV^{2+} cations can engage in a photoinduced electron transfer from a nanocrystal provided that the semiconductor conduction band edge lies above that of V^{2+} LUMO level (e.g. CdS[39]). If the charge transfer process is sufficiently fast, it leads to quenching of the band gap photoluminescence in nanocrystals with the quenching efficiency determined by the number of MV^{2+} attachment sites and the nature of surface adsorption. In this study, an equilibrium regime of MV^{2+} binding to nanocrystal surfaces was achieved by requiring the cessation of changes in the emission spectra of nanocrystal/MV^{2+} mixture during stirring of an analyte with a nanocrystal chloroform solution. Removing MV^{2+} from solution *via* precipitation and re-dissolution of nanocrystals resulted in a partial restoration of the PL signal indicating that not all MV^{2+} cations were stoichimetrically bound to the surface.

The MV^{2+} concentration dependence of the two emission peaks in PbS/CdS/CdSe is plotted in Fig. 5b. With the increasing amount of MV^{2+} adsorbed on nanoparticle surfaces, the emission of the PbS core becomes considerably reduced, while the emission of the CdSe shell subsides only by about 50%. The corresponding PbS-to-CdSe emission intensity ratio in Fig. 5e clearly reflects this trend. The stronger quenching of the PbS emission implies that the PbS($1S_e$) → MV^{2+} electron transfer is more efficient than the competing CdSe($1S_e$) → MV^{2+} electron injection process despite a PbS domain being separated from MV^{2+} by a small potential barrier of CdS. Namely, photoinduced electrons were more efficiently scavenged from the PbS core domain than from the CdSe shell to which MV^{2+} molecules were directly adsorbed. This unusual behavior could be attributed to two possible reasons: a greater driving force for an electron transfer from PbS to MV^{2+} and the difference in PL lifetimes between PbS and CdSe excited states that favors a slow non-radiative process to quench the PbS emission at a greater rate. The driving force consideration is supported by the cyclic voltammetry measurements of CdS-MV^{2+} complexes that place the expected LUMO level of V^{2+} just slightly below the CdS band edge.[39] Accordingly, the V^{2+} LUMO can be tentatively positioned between CB levels of PbS and CdSe domains (Fig. 5a), which would favor the electron transfer from PbS. Secondly, even if the CdSe → MV^{2+} electron transfer process outpaces PbS(e)→MV^{2+}, the 20-fold difference in the lifetime of PbS and CdSe excitons (see Figs. 2c & 2d) will result in the preferential suppression of the PbS emission. Consequently, the decrease in the PbS/CdSe emission ratio can be attributed to the difference in PbS and CdSe exciton lifetimes and more favorable PbS → MV^{2+} energetics.

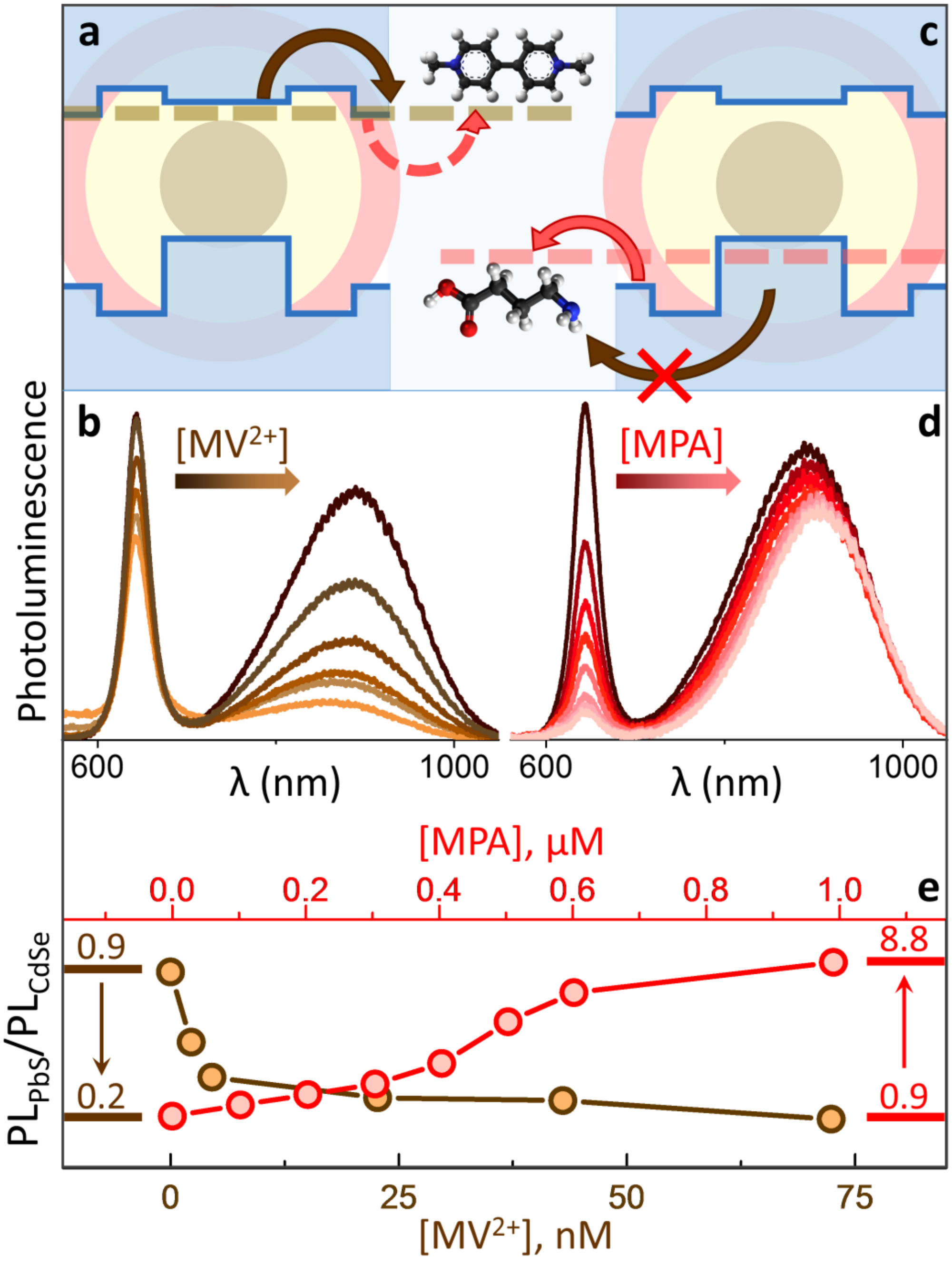

Figure 5. (a,b) Methyl viologen concertation dependence of the dual-color emission in PbS/CdS/CdSe NCs. PbS band gap photoluminescence is quenched at a greater rate than that of CdSe due to a shorter

CdSe exciton lifetime and potentially less favorable position of the CB_{CdSe} energy level relative to MV^{2+} LUMO. (c, d). The effect of MPA binding on the emission of PbS/CdS/CdSe NCs. CdSe band gap photoluminescence is quenched at a greater rate than that of PbS due to a more favorable CdSe (1Sh) → MV^{2+} energetics. (e). PbS-to-CdSe emission ratio *versus* the concentrations of MV^{2+} (brown curve, bottom scale markers) and MPA (red curve, top scale markers) molecules in chloroform.

A hole scavenging agent, 3-Mercaptopropionic acid (MPA), was employed as a representative example of an anionic molecule. [40,41] Similar to MV^{2+}, MPA was introduced to a chloroform solution of nanocrystals at various concentrations and the mixture was stirred until the changes in the emission profile were no longer observed. Binding of MPA thiol group to nanocrystals promotes CdSe ($1S_h$)→MPA hole transfer causing PL quenching. The trend is clearly seen in the photoluminescence spectra of MPA/nanocrystal mixture (Fig. 5d) showing a noticeable reduction in the intensity of the CdSe emission band. Notably, the emission of the PbS core remained largely unchanged causing the corresponding PbS-to-CdSe emission intensity ratio in Fig. 5e to grow with increasing MPA concertation. Considering that an exciton lifetime is 20 times longer in a PbS domain, quenching of the PL signal in CdSe indicates that the rate of hole transfer from CdSe ($1S_h$) to MPA is far greater than PbS ($1S_h$) → MPA. Consequently, CdSe ($1S_h$) → MPA must be energetically more favorable (greater driving force). Indeed the fact that HOMO level of MPA is situated above the VB edge of CdSe has been confirmed by numerous reports on CdSe→MPA hole transfer dynamics.[42,43] It is also well known that the VB of PbS is located above MPA HOMO level, as PL lifetime of small-diameter MPA-caped PbS NCs (τ = 220 ns)[44] does not differ significantly from that of OA-capped PbS NCs (τ = 380 ns). Along these lines, the MPA HOMO was tentatively placed between valence band (VB) edges of PbS and CdSe domains, as shown in Fig. 5c to explain a selective quenching of the CdSe PL signal. It should be noted that the high potential of PbS holes ensures that the PbS signal is unaffected during concentration depended quenching of the CdSe emission. This scenario offers an important benefit, as the constancy of the PbS PL signal makes the CdSe-to-PbS emission ratio change in a predictable manner with the increasing concentration of MPA. The reference signal provided by the PbS emission can thus facilitate quantifying the concentration of MPA (or thiols in general) in solution.

In summary, we report on the synthesis of dual–emitting PbS/CdS/CdSe core/barrier/shell nanocrystals supporting zero-dimensional excitons in the core and two-dimensional excitons the shell domains. By employing an interstitial CdS barrier at the PbS/CdSe interface, it was possible to suppress interactions between the core and shell excitations, which was manifested through a bright photoluminescence from both PbS and CdSe spectral bands. The corresponding PL peak positions were independently tunable *via* a domain size across 600-650 and 880-1800 nm spectral windows, respectively. Fabricated colloids were demonstrated as dual-color probes for sensing the redox environment, where both the energetics and the timing of the photoinduced charge transfer to an add-on analyte could be inferred from the ratiometric measurements.

Supporting information. Experimental section, additional figures and details of calculation. This material is available free of charge via the Internet at http://pubs.acs.org.

Acknowledgment. This work was supported by the Award DE-SC0016872 (MZ) funded by the U.S. Department of Energy, Office of Science. PM was supported in part by the NSF DMR-1710063 Award.

References.

---

[1] Chen, S.; Hong, Y.; Liu, Y.; Liu, J.; Leung, C. W. T.; Li, M.; Kwok, R. T. K.; Zhao, E.; Lam, J. W. Y.; Yu, Y.; Tang, B. Z. Full-Range Intracellular pH Sensing by an Aggregation-Induced Emission-Active Two-Channel Ratiometric Fluorogen. *J. Am. Chem. Soc*. **2013**, *135*, 4926-4929.

[2] Miesenbock, G.; De Angelis, D. A.; Rothman, J. E. Visualizing secretion and synaptic transmission with pH-sensitive green fluorescent proteins. *Nature* **1998**, *394*, 192-195.

[3] Niu, C.-G.; Gui, X.-Q.; Zeng, G.-M.; Guan, A.-L.; Gao, P.-F.; Qin, P.-Z. Fluorescence ratiometric pH sensor prepared from covalently immobilized porphyrin and benzothioxanthene. *Anal. Bioanal. Chem.* **2005**, *383*, 349-357.

[4] Medintz, I. L.; Stewart, M. H.; Trammell, S. A.; Susumu, K.; Delehanty, J. B.; Mei, B. C.; Melinger, J. S.; Blanco-Canosa, J. B.; Dawson, P. E.; Mattoussi, H. Quantum-dot/dopamine bioconjugates function as redox coupled assemblies for in vitro and intracellular pH sensing. *Nat. Mater.* **2010**, *9*, 676-684.

[5] Dennis, A.M.; Rhee, W.J.; Sotto, D.; Dublin, S.N.; Bao, G. Quantum Dot–Fluorescent Protein FRET Probes for Sensing Intracellular pH. *ACS Nano*, **2012**, *6*, 2917–2924.

[6] Lorenzon, M.; Pinchetti, V.; Bruni, F.; Bae, W. K.; Meinardi, F.; Klimov, V. I.; Brovelli, S. Single-Particle Ratiometric Pressure Sensing Based on “Double-Sensor” Colloidal Nanocrystals. *Nano Lett.*, **2017**, *17*, 1071–1081.

[7] McLaurin, E. J.; Vlaskin, V. A.; Gamelin, D. R. Water-Soluble Dual-Emitting Nanocrystals for Ratiometric Optical Thermometry. *J. Am. Chem. Soc.* **2011**, *133*, 14978–14980.

[8] Albers, A. E.; Chan, E. M.; McBride, P. M.; Ajo-Franklin, C. M.; Cohen, B. E.; Helms, B. A. Dual-Emitting Quantum Dot/Quantum Rod-Based Nanothermometers with Enhanced Response and Sensitivity in Live Cells. *J. Am. Chem. Soc.* **2012**, *134*, 9565–9568.

[9] Vlaskin, V. A.; Janssen, N.; van Rijssel, J.; Beaulac, R.; Gamelin, D. R. Tunable Dual Emission in Doped Semiconductor Nanocrystals. *Nano Lett.* **2010**, *10*, 3670-3674.

[10] Lin, Q.; Makarov, N. S.; Koh, W.-K.; Velizhanin, K. A.; Cirloganu, C. M.; Luo, H.; Klimov, V. I.; Pietryga, J. M. Design and Synthesis of Heterostructured Quantum Dots with Dual Emission in the Visible and Infrared. *ACS Nano* **2015**, *9*, 539–547.

---

[11] Bruni, F.; Pedrini, J.; Bossio, C.; Santiago-Gonzalez, B.; Meinardi, F.; Bae, W. K.; Brovelli, S. Two-Color Emitting Colloidal Nanocrystals as Single-Particle Ratiometric Probes of Intracellular pH. *Adv. Funct. Mater.* **2017**, *27*, 1605533.

[12] Galland, C.; Brovelli, S.; Bae, W. K.; Padilha, L. A.; Meinardi, F.; Klimov, V. I. Dynamic Hole Blockade Yields Two-Color Quantum and Classical Light from Dot-in-Bulk Nanocrystals. *Nano Lett.* **2013**, *13*, 321–328.

[13] Zhao, H.; Sirigu, G.; Parisini, A.; Camellini, A.; Nicotra, G.; Rosei, F.; Morandi, V.; Zavelani-Rossih, M.; Vomiero, A. Dual emission in asymmetric "giant" PbS/CdS/CdS core/shell/shell quantum dots. *Nanoscale*, **2016**, *8*, 4217–4226.

[14] Zhao, H. G.; Wu, N.; Chaker, M.; Ma, D. Towards controlled synthesis and better understanding of highly luminescent PbS/CdS core/shell quantum dots. *J. Mater. Chem.* **2011**, *21*, 8898–8904.

[15] Choi, C. L.; Li, H.; Olson, A. C. K.; Jain, P. K.; Sivasankar, S.; Alivisatos, A. P. Spatially Indirect Emission in a Luminescent Nanocrystal Molecule. *Nano Lett.* **2011**, *11*, 2358–2362.

[16] Zhao, H. G.; Liang, H. Y.; Gonfa, B. A.; Chaker, M.; Ozaki, T.; Tijssen, P.; Vidal, F.; Ma, D. Investigating photoinduced charge transfer in double- and single-emission PbS@CdS core@shell quantum dots. *Nanoscale*, **2014**, *6*, 215–225.

[17] Lutich, A. A.; Mauser, C.; Da Como, E.; Huang, J.; Vaneski, A.; Talapin, D. V.; Rogach, A. L.; Feldmann, J. Multiexcitonic Dual Emission in CdSe/CdS Tetrapods and Nanorods. *Nano Lett.*, **2010**, *10*, 4646–4650.

[18] Pinchetti, V.; Meinardi, F.; Camellini, A.; Sirigu, G.; Christodoulou, S.; Bae, W. K.; De Donato, F.; Manna, L.; Zavelani-Rossi, M.; Moreels, I.; Klimov, V.I.; Brovelli, S. Effect of Core/Shell Interface on Carrier Dynamics and Optical Gain Properties of Dual Color Emitting CdSe/CdS Nanocrystals. *ACS Nano* **2016**, *10*, 6877−6887.

[19] Battaglia, D.; Blackman, B.; Peng, X. Coupled and Decoupled Dual Quantum Systems in One Semiconductor Nanocrystal. *J. Am. Chem. Soc.* **2005**, *127*, 10889−10897.

[20] Nizamoglu, S.; Mutlugun, E.; Özel, T.; Demir, H. V.; Sapra, S.; Gaponik, N.; Eychmüller, A. Dual-Color Emitting Quantum-DotQuantum-Well CdSe-ZnS Heteronanocrystals Hybridized on InGaN/GaN Light Emitting Diodes for High-Quality White Light Generation. *Appl. Phys. Lett.* **2008**, *92*, 113110.

---

[21] Dias, E. A.; Grimes, A. F.; English, D. S.; Kambhampati, P. Single Dot Spectroscopy of Two-Color Quantum Dot/Quantum Shell Nanostructures. *J. Phys. Chem. C* **2008**, *112*, 14229−14232.

[22] Zaiats, G.; Kinge, S.; Kamat, P. V. Origin of Dual Photoluminescence States in ZnS–$CuInS_2$ Alloy Nanostructures. *J. Phys. Chem. C* **2016**, *120*, 10641–10646.

[23] Deutsch, Z.; Schwartz, O.; Tenne, R.; Popovitz-Biro, R.; Oron, D. Two-Color Antibunching from Band-Gap Engineered Colloidal Semiconductor Nanocrystals. *Nano Lett.* **2012**, *12*, 2948–2952.

[24] Kuno, M. Tailoring the Inherent Optical and Electrical Properties of Nanostructures. *J. Phys. Chem. Lett.* **2014**, 5 (21), 3817-3818.

[25] Wei, H. H.-Y.; Evans, C. M.; Swartz, B. D.; Neukirch, A. J.; Young, J.; Prezhdo, O. V. Krauss, T. D. Colloidal Semiconductor Quantum Dots with Tunable Surface Composition. *Nano Lett.* **2012**, *12*, 4465-4471.

[26] McLaurin, E. J.; Fataftah, M. S.; Gamelin, D. R. One-step synthesis of alloyed dual-emitting semiconductor nanocrystals. *Chem. Commun.* **2013**, *49*, 39-41.

[27] Deng, Z.; Tong, L.; Flores, M.; Lin, S.; Cheng, J.-X.; Yan, H.; Liu, Y. High-Quality Manganese-Doped Zinc Sulfide Quantum Rods with Tunable Dual-Color and Multiphoton Emissions. *J. Am. Chem. Soc.*, **2011**, *133*, 5389–5396.

[28] Hsia, C.-H.; Wuttig, A.; Yang, H. An Accessible Approach to Preparing Water-Soluble Mn2+-Doped (CdSSe)ZnS (Core)Shell Nanocrystals for Ratiometric Temperature Sensing. *ACS Nano*, **2011**, *5*, 9511–9522.

[29] McLaurin, E. J.; Bradshaw, L. R.; Gamelin, D. R. Dual-Emitting Nanoscale Temperature Sensors. *Chem. Mater.* **2013**, *25*, 1283–1292.

[30] Zheng, J.; Cao, S.; Wang, L.; Gao, F.; Wei, G.; Yang, W. Temperature-dependent photoluminescence properties of Mn:ZnCdS quantum dots. *RSC Adv.*, **2014**, *4*, 30948-30952.

[31] Razgoniaeva, N.; Moroz, P.; Yang, M.; Budkina, D. S.; Eckard, H.; Augspurger, M.; Khon, D.; Tarnovsky, A. T.; Zamkov, M. One-dimensional carrier confinement in “giant” CdS/CdSe excitonic nanoshells. *J. Am. Chem. Soc.* **2017**, *139*, 7815-7822.

[32] Pietryga, J. M.; Werder, D. J.; Williams, D. J.; Casson, J. L.; Schaller, R. D.; Klimov, V. I.; Luther, J. A. Utilizing the Lability of Lead Selenide to Produce Heterostructured Nanocrystals with Bright, Stable Infrared Emission. *J. Am. Chem. Soc.* **2008**, *130*, 4879-4885.

---

[33] Moroz, P.; Liyanage, G.; Kholmicheva, N.; Yakunin, S.; Uprety, P.; Bastola, E.; Rijal, U.; Mellott, B.; Subedi, K.; Sun, L.; Kovalenko, M.V.; Zamkov, M. Infrared Emitting PbS Nanocrystal Solids through Matrix Encapsulation. *Chem. Mater*. **2014**, *26*, 4256-4264.

[34] Fang, H.-H.; Balazs, D. M.; Protesescu, L.; Kovalenko, M. V.; Loi, M. A. Temperature-Dependent Optical Properties of PbS/CdS Core/Shell Quantum Dot Thin Films: Probing the Wave Function Delocalization. *J. Phys. Chem. C*, **2015**, *119*, 17480–17486.

[35] Justo, Y.; Geiregat, P.; Van Hoecke, K.; Vanhaecke, F.; De Mello Donega, C.; Hens, Z. Optical Properties of PbS/CdS Core/Shell Quantum Dots. *J. Phys. Chem. C*, **2013**, *117*, 20171–20177.

[36] X. Ji, G. Palui, T. Avellini, H-B. Na, C-Y. Yi, K.L. Knappenberger Jr., and H. Mattoussi, On the pH-Dependent Quenching of Quantum Dot Photoluminescence by Redox Active Dopamine. *J. Am. Chem. Soc.*, **2012**, *134*, 6006−6017.

[37] Lechner, R.T.; Fritz-Popovski, G.; Yarema, M.; Heiss, W.; Hoell, A.; Schülli, T. U.; Primetzhofer D.; Eibelhuber, M.; Paris. O. Crystal Phase Transitions in the Shell of PbS/CdS Core/Shell Nanocrystals Influences Photoluminescence. *Chem. Mater.*, **2014**, *26*, 5914–5922.

[38] Peterson, M. D.; Jensen, S. C.; Weinberg D. J.; Weiss, E. A. Mechanisms for Adsorption of Methyl Viologen on CdS Quantum Dots. *ACS Nano*, **2014**, *8*, 2826–2837.

[39] Morris-Cohen, A. J.; Frederick, M. T.; Cass, L. C.; Weiss, E. A. Simultaneous Determination of the Adsorption Constant and the Photoinduced Electron Transfer Rate for a CdS Quantum Dot Viologen Complex. *J. Am. Chem. Soc.* **2011**, *133*, 10146–10154.

[40] Wuister, S. F.; Donega, C. D.; Meijerink, A. Influence of Thiol Capping on the Exciton Luminescence and Decay Kinetics of CdTe and CdSe Quantum Dots *J. Phys. Chem. B* **2004**, *108*, 17393–17397.

[41] Acharya, K.; Khnayzer, R. S.; O'Connor, T.; Diederich, G.; Kirsanova, M.; Klinkova, A.; Roth, D.; Kinder, E.; Imboden, M.; Zamkov, M. The role of hole localization in sacrificial hydrogen production by semiconductor–metal heterostructured nanocrystals. *Nano Lett.* **2011**, *11*, 2919–2926.

[42] Amirav, L.; Alivisatos, P. A. Photocatalytic Hydrogen Production with Tunable Nanorod Heterostructures. *J. Phys. Chem. Lett.*, **2010**, *1*, 1051.

[43] Khon, E.; Lambright, K.; Khnayzer, R.S.; Moroz, P.; Perera, D.N.; Butaeva, E.; Lambright, S.; Castellano, F.N.; Zamkov, M. Improving the Catalytic Activity of Semiconductor Nanocrystals through Selective Domain Etching. *Nano Lett.*, **2013**, *13*, 2016-2023.

---

[44] Moroz, P.; Kholmicheva, N.; Mellott, B.; Liyanage, G.; Rijal, U.; Bastola, E.; Huband, K.; Khon, E.; McBride, K.; Zamkov, M. Suppressed Carrier Scattering in CdS-Encapsulated PbS Nanocrystal Films. *ACS Nano* **2013**, *7*, 6964-6977.